HEFAT2010
7th International Conference on Heat Transfer, Fluid Mechanics and Thermodynamics
19-21 July 2010
Antalya, Turkey

TRANSIENT FLOW IN A THERMOSYPHON INCLINED AT 30°

Ho M. and Leong S.S.*
*Author for correspondence
School of Mechanical and Manufacturing Engineering
The University of New South Wales
Sydney, 2052
Australia
E-mail: s.leong@unsw.edu.au

ABSTRACT

The time dependent natural convection in an inclined closed thermosyphon with the lower ¾ surface isothermally heated and the upper ¼ surface isothermally cooled is investigated. The vertical temperature gradient creates a buoyancy-driven flow in the cylinder. Depending on the Rayleigh number *Ra*, the resulting natural convection can be simple or complex three-dimensional flow structures.

The three-dimensional time-dependent Navier-Stokes equations (with Boussinesq approximation) for an incompressible viscous fluid are approximated using finite-differences. The energy and vorticity transport equations are solved using a modified alternating direction implicit scheme. The elliptic equation for the vector-potential is solved directly using a fast Fourier transform algorithm.

Numerical results are presented for an aspect ratio (length to radius) of 4. A Prandtl number of 7 is used for the fluid. The time-dependent flow structures, total kinetic energy within the cylinder and heat transferred are presented for various values of Rayleigh number.

INTRODUCTION

Convection phenomena driven by thermally induced buoyancy forces present applications in thermal engineering. Japikse [1971] reviewed the use of thermosyphons as heat exchange devices including gas turbine blade cooling, transformer cooling and cooling of nuclear reactors.

Considerable research has been directed to closed thermosyphons in 2-D and 3-D geometries. The collective studies on the effects of boundary layer interactions, aspect ratios, fluid properties and three-dimensionality have been reviewed by Fusegi and Hyun [1993] and Ostrach [1988]. Hsieh and Yang [1996] noted that the complex 3-D flows are not effectively captured by numerical studies in 2-D geometries.

Numerical models available for cylindrical tubes are limited, largely in part due to complications involving singularity along the axis. Transient solutions were undertaken by Leong [2009] for a vertical case, where complex cross-over flow in figure '8' formations formed across the mid-plane.

The relative simplicity of inducing inclination makes the parameter a critical point of interest for stability and heat transfer determination. Lock & Kirchner [1988] and Japikse et al. [1971] experimentally studied the effect of minor inclinations on cylindrical thermosyphons. The formation of two opposing streams that accompanies increasing inclination was observed.

In the present study, the numerical results will be presented for a cylinder inclined at 30 degrees with isothermal heating of the lower three-quarter (¾) region, and cooling of the upper quarter (¼). The cylinder has an aspect ratio of (*a*=length/radius) of 4 and contains fluid of Prandtl number (*Pr*) 7.

The specific temperature boundary conditions poses more realistic boundary conditions than differentially heated vertical walls and adiabatic end wall problems (de Vahl Davis et al. [1983]; Ozoe et al. [1985]; Sammouda et al. [1999]). In the later problem type, prior research indicates that maintaining perfectly adiabatic end walls can be difficult in industrial applications (Gaa et al. [1998]). In contrast, a fluid-filled cylinder partially submerged in a hot body (e.g. nuclear reactor core) and exposed in the upper section to a cooler environment can be modelled by the selected boundaries.

NOMENCLATURE

a	aspect ratio, *R*/*H*
H	height of cylinder
KE	relative kinetic energy
L	number of radial mesh points
M	number of azimuthal mesh points
N	number of axial mesh points

Nu	Nusselt number
Pr	Prandtl number
R	radius of cylinder
Ra	Rayleigh number
r	radial coordinate
$\bar{u}$	velocity vector
u	radial velocity
v	azimuthal velocity
w	axial velocity
θ	dimensionless temperature
υ	kinematic viscosity
κ	thermal diffusivity
$\bar{\psi}$	vector potential
$\bar{\zeta}$	vorticity vector

Subscripts

h	hot
c	cold
ϕ	azimuthal component

GOVERNING EQUATIONS

The energy and momentum equations are non-dimensionalised using R (radius of the cylinder), R^2/κ and κ/R as scale factors for length, time and velocity respectively. κ is the fluid thermal diffusivity. Applying the Boussinesq approximation, the energy and vorticity transport equations are given by:

$$\frac{\partial\theta}{\partial t} = -\nabla\cdot\left(\bar{u}T\right) + \kappa\nabla^2\theta \tag{1}$$

$$\frac{\partial\bar{\zeta}}{\partial t} = \nabla\times\left(\bar{u}\times\bar{\zeta}\right) - Ra\cdot\mathrm{Pr}\nabla\times\left(\theta\bar{g}\right) - \mathrm{Pr}\nabla\times\left(\nabla\times\bar{\zeta}\right) \tag{2}$$

where $\theta=(T-T_0)/\Delta T$ is the dimensionless temperature, $T_0=(T_h+T_c)/2$, $\Delta T=(T_h-T_c)$ and T_h and T_c are the temperature at the hot and cold walls respectively. $\bar{\zeta}$ is the vorticity vector, $Pr=\upsilon/\kappa$ is the Prandtl number, $Ra=\beta g(T_h-T_c)R^3/\upsilon\kappa$ is the Rayleigh number and υ is the kinematic viscosity. The components of the velocity vector $\bar{u}$ are u, v and w in the radial (r), azimuthal (ϕ) and axial (z) directions respectively. The velocity vector is evaluated from solenoidal vector potential field $\bar{\psi}$, which satisfies the continuity equation and the curl of which gives the velocity field, that is:

$$\nabla\cdot\bar{\psi} = 0 \tag{3}$$

$$\bar{u} = \nabla\times\bar{\psi} \tag{4}$$

The relationship between vorticity $\bar{\zeta}$ and vector potential $\bar{\psi}$ is given by:

$$\bar{\zeta} = \nabla\times\bar{u} = \nabla\times\left(\nabla\times\bar{\psi}\right) \tag{5}$$

BOUNDARY CONDITIONS

The fluid has zero velocities at the rigid walls ($u=v=w=0$). The thermal boundary conditions are $\theta=0.5$ at $0\le z<3a/4$, $\theta=0$ at $z=3a/4$ and $\theta=-0.5$ at $3a/4<z\le a$.

NUMERICAL SOLUTION

A uniform cylindrical mesh distribution over the cylinder consists of $L\times M\times N$ discrete points in the r, ϕ and z directions respectively. The radial mesh points are given by $r_i=(i-1/2)\Delta r$ for $i=1,2,3,...L$; the azimuthal mesh points are given by $\phi_j=(j-1)\Delta\phi$ for $j=1,2,3,...M$ and the axial mesh points are given by $z_k=(k-1)\Delta z$ for $k=1,2,3,...N$, where $\Delta r=1/(L-1/2)$, $\Delta\phi=2\pi/M$ and $\Delta z=a/(N-1)$. Finite different approximations are used to solve (1) and (2). Second order forward differences are necessary to solve along the circumferential boundary at $r=\Delta r/2$. The resulting finite difference equations are then solved by a modified Samarskii-Andreyev Alternating Direction Implicit (ADI) at each time-step. The elliptic equation (5) is solved directly by a Fast Fourier Transform.

MESH VALIDATION

Three different time-steps of 5×10^{-5}, 1×10^{-5} and 5×10^{-6} are tested for the mesh sizes $17\times32\times33$, $17\times64\times65$ and $21\times64\times65$. The transient KE plots in Figure 1 show reasonable agreement between the various meshes and time-steps. The KE values at steady state are the same for equal number of mesh points in the axial direction. This demonstrates that a finer axial mesh choice improves the solution more than smaller time-step selections. The steady state values for KE are higher at $N=65$ than $N=32$ due to additional heating and cooling at the longitudinal walls for the finer mesh.

The error term is effectively zero for mesh sizes finer than $21\times64\times65$ and time-steps smaller than 5×10^{-5}, indicating that the independence condition has been reached at these values. Therefore, for lower Ra ($Ra<2\times10^4$), a mesh of $17\times64\times65$ is sufficiently accurate at a time-step 5×10^{-5}.

RESULTS

Solutions are obtained for Prandtl number $Pr=7$, Rayleigh number $700\le Ra\le4\times10^5$, and aspect ratio $a=4$. Temperature (θ) isotherms and angular component of vector potential (ψ_ϕ) in the secondary ($\phi=0,\pi$) planes are illustrated in Figure 2. The contour plots show the range of contour levels and the number of contour levels [*min, max, no. of levels*]. Dashed lines along contour boundaries indicate negative values.

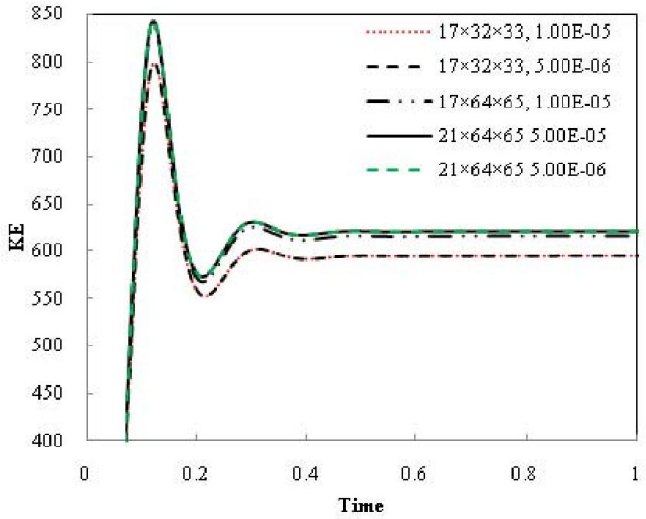

Figure 1 Transient plots of KE for Ra=700 for various mesh sizes and time-steps

θ and ψ_ϕ are axisymmetric in the secondary plane. θ contours spread longitudinally in an elliptical formation. From Figure 2b, ψ_ϕ illustrates two pairs of counter rotating vortices separated by the heat exchange region.

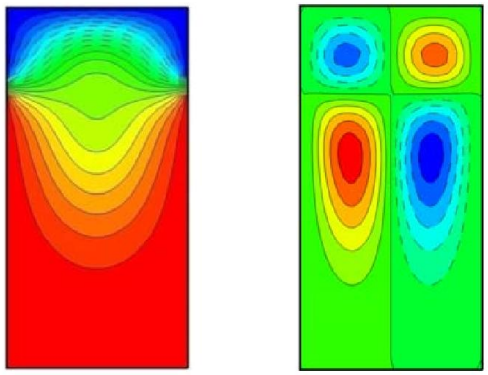

(a) θ[-0.5,0.5,11] (b) ψ_ϕ[-0.5, 0.5, 11]

Figure 2 Secondary plane plots of θ *and* ψ_ϕ at steady state for Ra=700

The dominant flow structure consisting of $\psi_{\phi,\ min}$=-4.6 in Figure 3a is asymmetric and exists in the primary plane (ϕ=π/2, 3π/2). At Ra=700, incipient stages of a unicellular vortex consist of a weak ascending stream rising along the hot leading side towards the end wall and an opposing stream along the lower (trailing) wall. The pairs of rotating cells in the secondary plane indicate cross-over flow between coupled streams, occurring towards the axis and laterally in line with the heat exchange region. In effect, this phenomenon shares cross-over characteristics with the figure '8' structures observed by Ishihara et al. [2002] and Leong [2009] in vertical thermosyphons.

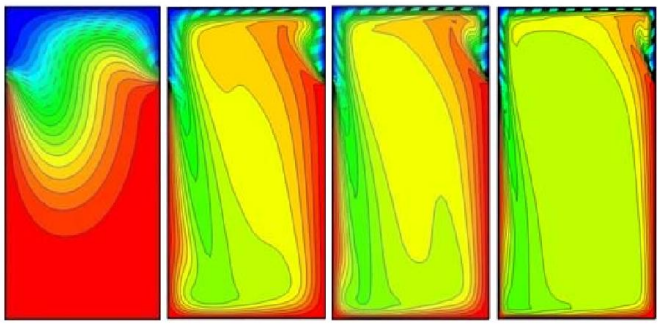

(a) Ra=700 (b) Ra=2×10^4 (c) Ra=5×10^4 (d) Ra=4×10^5

Figure 3 Plots of θ[-0.5,0.5,11] at steady state

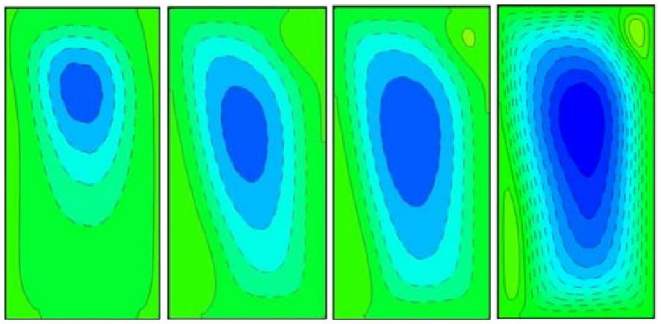

(a) Ra=700 ψ_ϕ[-4,0,5] (b) Ra=2×10^4 ψ_ϕ[-40,0,5] (c) Ra=5×10^4 ψ_ϕ[-60,15,6] (d) Ra=4×10^5 ψ_ϕ[-160,32,13]

Figure 4 Plots of ψ_ϕ at steady state

The axial velocity Figure 5 is therefore positive on the right leading wall and negative on the trailing wall. When the flow becomes steady, axial velocity at z=3a/4 is larger than at z=7a/8 demonstrating deceleration of the rising stream. The two-stream behaviour, referred to herein as *bifilamental flow*, is commonly observed in inclined geometries with circular (Japikse et al. [1971]; Lock and Kirchner [1988]; Gaa et al [1997]) or rectangular (Lock and Zhao [1990]) cross-sections.

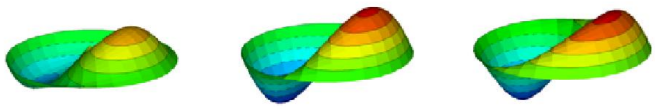

(a) z=7a/8 (b) z=3a/4 (c) z=5a/8

Figure 5 Cross-sections plots of axial velocity w[-10,8,10] at steady state for Ra=700

The main flow structure in the primary plane persists for Ra=2×10^4 with the intensity of the bifilamental flow increasing. θ isotherms increase in density along the boundaries, forming a boundary layer along the longitudinal walls as shown in Figure 3b. The hot boundary layer is thicker along the leading edge,

which encourages upward movement of the ascending stream (Figure 4b).

The flow for $5x10^4 \leq Ra \leq 2.8x10^5$ is similar to the fields observed in $Ra=2x10^4$ albeit with increasing intensity. Within this range, a secondary clockwise (CW) cell initially forms in the upper right corner at $Ra=5x10^4$ (Figure 4c), with a further cell accompanying higher Ra in the lower left-corner at (Figure 4d). The two CW cells form at the end-points of the opposing streams as the particles bifurcate upon collision with the end-wall.

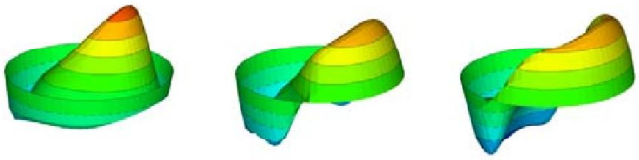

(a) $z=7a/8$ (b) $z=3a/4$ (c) $z=5a/8$

Figure 6 Cross-sections plots w[-160,160,9] at steady state for $Ra=5\times10^4$

Figure 6 shows the axial velocity plots at various cross-sections for $Ra=5x10^4$. As the rising stream passes the heat exchange region the particles deflect inwards towards the axis. The subsequent collision with the end-wall causes radial dispersal of flow, shown by the downward travelling annulus at $z=7a/8$. Japikse et al. [1971] noted similar end-wall behaviour caused opposing flow to form vortices in a cylinder. Lock and Zhao [1990] referred to this phenomenon as *refluent flow* and suggested this behaviour occurred above a critical Ra leading to the formation of a Bénard cell in which an upward core flow is balanced by a downward flow.

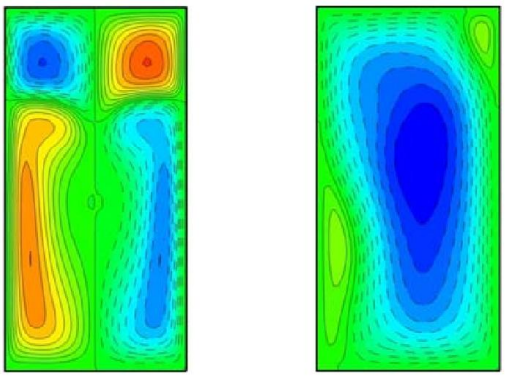

(a) Secondary Plane (b) Primary Plane

ψ_ϕ [-40, -40, 17] ψ_ϕ [-180, 36, 13]

Figure 7 Contour plots of ψ_ϕ for $Ra=4\times10^5$

At $Ra=4\times10^5$, the flow enters an oscillatory state with no convergence to steady state. ψ_ϕ in the secondary plane becomes increasingly distorted from the elliptic shapes observed in the laminar range. From Figure 7, the dominant vortex in the primary plane is similar to $Ra=2.8\times10^5$. However, the main flow becomes impeded near the end-walls due to the shifting CW cells in opposing corners (Figure 7b).

Figure 8 illustrates the transient behaviour of the axial velocity profile under unstable conditions. At $Ra=4\times10^5$, flow near the axis and at $z=3a/4$ is turbulent and forms a complex 3-D stagnation zone (Figure 8). The ascending stream has a distinct peak at all time intervals, suggesting a sustained structure consisting of a concentrated ascending stream.

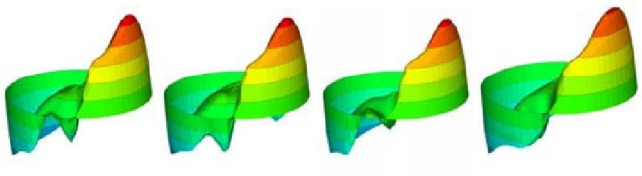

(a) $t=0.25$ (b) $t=0.50$ (c) $t=0.75$ (d) $t=1.00$

Figure 8 Axial velocity w[-600, 540, 10] at $z=3a/4$ for $Ra=4\times10^5$

Bifurcation of the primary stream upon collision with the end-wall is shown in Figure 9. The effect of the inclination is twofold; it destroys the axisymmetry in the primary plane and modifies the vortex structure at the end-wall. The ascending stream has sufficient inertia to penetrate to the top wall, where only a vestige remains in the stagnation region in the upper right corner of Figure 9b. The remaining flow sweeps across the end-wall to form the opposing stream on the trailing wall.

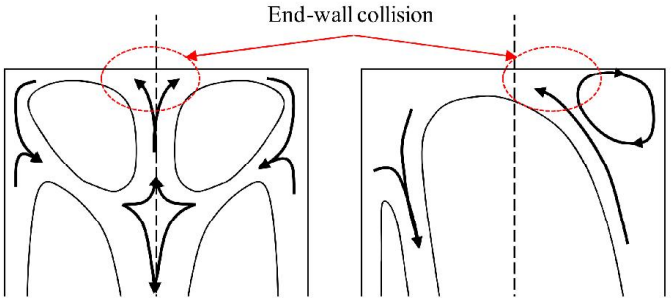

(a) Secondary (b) Primary

Figure 9 Refluent flow in the secondary and primary planes at end walls under inclined conditions

Plots of Nu against Ra are shown in Figures 10, 11 and 12. At low Ra the system reaches steady state consisting of constant heat transfer from the hot wall to cold wall. As Ra increases to $Ra=5\times10^4$, initial oscillations occur in the interval $0 \leq t \leq 0.17$. Figure 11 shows the Nu as a function of time for $5\times10^4 \leq Ra \leq 2.8\times10^5$. The oscillations increase as Ra increases. As seen in Figure 11, the Nu reaches steady state by $t=0.419$ for $Ra=2.8\times10^5$.

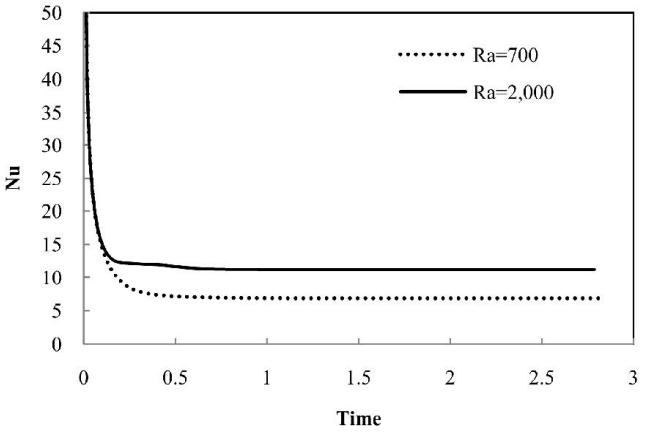

Figure 10 Transient plots of *Nu* for Ra=700, 2×10^3

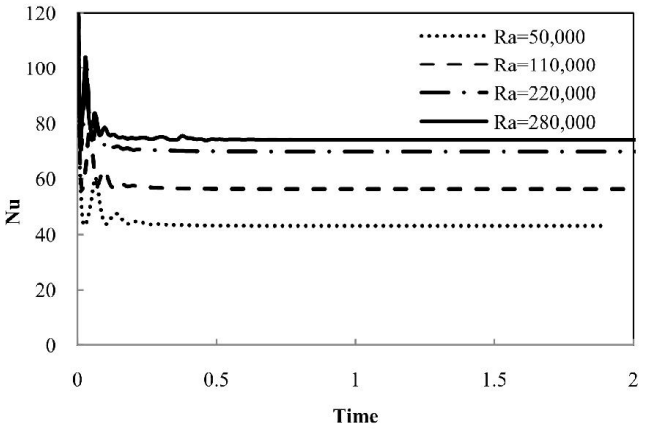

Figure 11 Transient plots of *Nu* for Ra=5×10^4, Ra=1.1×10^5, Ra=2.8×10^5

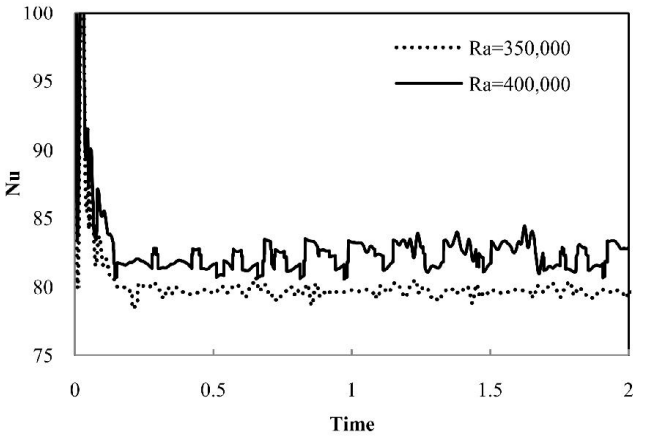

Figure 12 Transient plots of *Nu* for Ra=3.5×10^5, Ra=4×10^5

Figure 12 shows that there is no steady state solution at $Ra\geq3.5\times10^5$. This represents the transition into the turbulent oscillatory region of flow, and corresponds to the bifilamental flow with pockets of instability as seen in Figure 8 and Figure 9.

KEY TRENDS

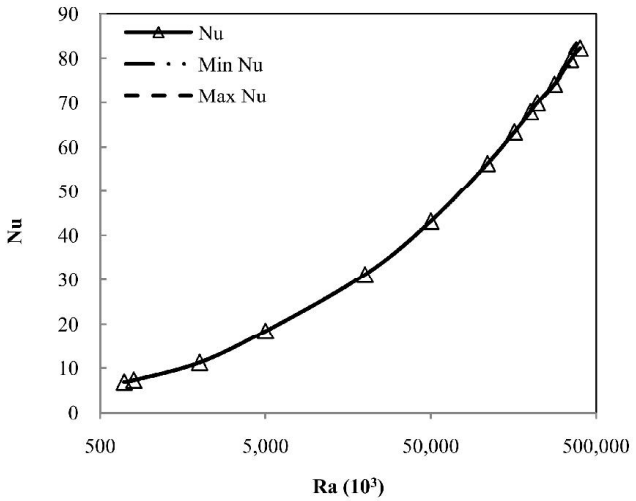

Figure 13 Average *Nu* as a function of *Ra*

The relationship between *Nu* and *Ra* is non-linear. The relationship is more effectively portrayed as a monotonically upward *Nu* versus Log(*Ra*) plot in Figure 13. At $Ra\leq2{,}000$, heat transfer increases marginally as a result of the superposition of conduction and incipient convection. As the boundary layer forms at $Ra\geq2\times10^4$, the curve becomes approximately linear. Average heat transfer in the turbulent regime ($Ra\geq3.5\times10^5$) becomes increasingly erratic due to the unsteady oscillations for the transient plots. *KE* and *Nu* values during the turbulent region or obtained by averaging the transient values in the interval $0.5\leq t\leq2.0$. Nevertheless, it is clear that a heat transfer rate is sensitive to *Ra*. Further increases to *Nu* are limited by the convergence of the temperature gradient along the curved wall boundary layers as *Ra* increases.

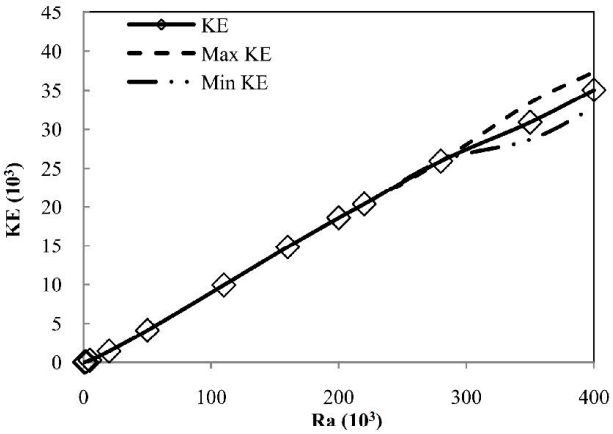

Figure 14 Average *KE* as a function of *Ra*

Steady state values for *KE* are plotted against *Ra* in Figure 14. A linear correlation exists between *KE* and *Ra* over the laminar-convective region of *Ra*. Sustained oscillations commence above a critical *Ra* $2.8\times10^5<Ra_{crit}<3.5\times10^5$, which eventually leads to increasing amplitudes as *Ra* increases. The spreading of the dotted lines, representing minimum and maximum *KE* in the post-peak oscillatory period, confirms the turbulent range.

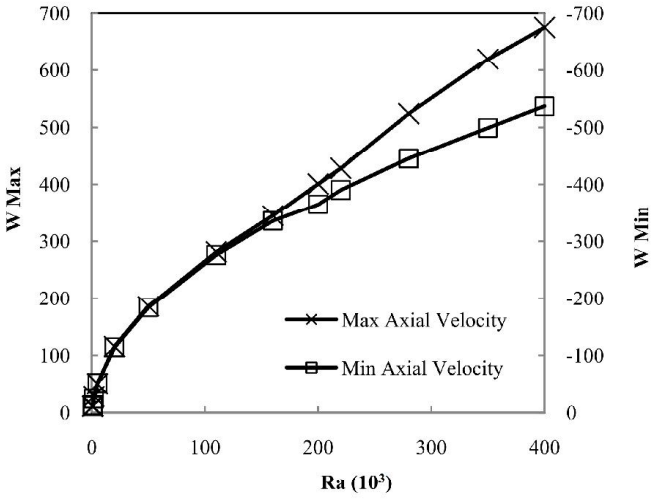

Figure 15 Axial velocity at $z=3a/4$ as a function of *Ra*

The maximum and minimum velocity values across the heat exchange region ($z=3a/4$) are shown in Figure 15. Axial velocity is maximum along the leading edge and positively correlated with *Ra*. The maximum negative flow falls away in magnitude compared to the positive curve at $Ra>1.6\times10^5$. As shown in Figure 8, the descending stream at high *Ra* forms from irregular refluent flow at the upper end wall. The instability causes the irregularity of the downward axial velocity profile and therefore limits the efficiency of the downward stream.

CONCLUSION

The collective results on modelling a variation of *Ra* at an angle of 30 degrees have shown that the flow progresses from incipient convection to turbulence. There was:

1. Superposition of incipient convection and conduction for $700\leq Ra\leq2\times10^3$;
2. Weak convection at $Ra=2\times10^4$;
3. Strong convection for $5\times10^4\leq Ra\leq2.8\times10^5$; and
4. Irregular oscillatory convection for $Ra\geq3.5\times10^5$.

The flow was found to depend on three key features: a two-stream formation in the core region referred to as bifilamental flow; end region behaviour where the streams collided with the walls to form refluent flow; and stream coupling which caused cross-over behaviour in the secondary plane. These characteristics were consistent with the experimental flow model developed by Lock and Kirchner [1988] and observations of Japikse et al. [1971]. The bifilamental flow consisted of a rising stream on the leading edge of the cylinder, and a descending stream along the trailing edge. At sufficiently high *Ra*, counter-rotating cells formed in opposing corners as a result of the stream colliding with the end-wall.

Ra had a large effect on heat transfer rates and *KE*. Heat transfer, in the form of *Nu*, was positively correlated with *Ra*, but at a decreasing rate. This was due to a convergence in the thickness of the boundary layer as *Ra* increased. Total *KE* increased linearly with respect to *Ra* over the laminar region. It was unclear whether the linearity extended into the turbulent region ($Ra\geq3.5\times10^5$) due to irregular oscillations over time.

REFERENCES

[1] de Vahl Davis, G. and Jones, I.P., 1983, 'Natural Convection in a Square Cavity: A Comparison Exercise', *Int. J. For Numerical Methods in Fluids*, vol. 3, pp. 227-248.

[2] Fusegi, T. and Hyun, J.M., 1993, 'Laminar and transitional natural convection in an enclosure with complex and realistic conditions', *Int. J. Heat and Fluid Flow*, vol. 15, no. 4, pp. 258-268.

[3] Gaa, F.O., Behnia, M., Leong, S.S. and Morrison, G.L., 1998, 'Numerical and experimental study of inclined open thermosyphons', *Intl. J. Numerical Methods for Heat and Fluid Flow*, vol. 8, no. 7, pp. 748-767.

[4] Hsieh, S.S. and Yang, S.S., 1996, 'Transient three-dimensional natural convection in a rectangular enclosure', *Int. J. Heat Mass Transfer*, vol. 39, no. 1, pp. 13-26.

[5] Ishihara, I., Fukui, T. and Matsumoto, R., 2002, 'Natural convection in a vertical rectangular enclosure with symmetrically localized heating and cooling zones', *Int. J. Heat and Fluid Flow*, vol. 23, pp. 366-372.

[6] Japikse, D., 1972, 'Advances in thermosyphon technology', *Advances in Heat Transfer*, vol. 19, pp. 1-111.

[7] Japikse, D., Jallouk, P.A. and Winter, E.R.F., 1971, 'Single-phase transport processes in the closed thermosyphon', *Int. J. Heat Mass Transfer*, vol. 14, pp. 869-887.

[8] Leong, S.S., 2009, 'Transient flow within a closed thermosyphon', paper presented to 6th International Conference on Computational Heat and Mass Transfer, Guangzhou, China, 18-21 May.

[9] Leslie, F.M., 1960, 'Free convection in the tilted open thermosyphon', *J. of Fluid Mechanics*, vol. 7, pp. 115-127.

[10] Lock, G.S.H and Kirchner, J.D., 1988, 'Flow and heat transfer in an inclined, closed tube thermosyphon', *Proc. National Heat Transfer Conf.*, ASME-HTD-96, vol. 3, pp, 205-215.

[11] Lock, G.S.H. and Zhao, L., 1990, 'The laminar flow field in a near vertical, closed tube thermosyphon', *Mathematical Computational Modelling*, vol. 14, pp. 822-825.

[12] Martin, B.W. and Lockwood, F.C., 1963, 'Entry effects in the open thermosyphon', J. Fluid Mechanics, vol. 19, no. 2, pp. 246-256.

[13] Ostrach, S., 1988, 'Natural convection in enclosures', *J. Heat Transfer*, vol. 110, pp. 175-1190.

[14] Ozoe, H., Mouri, A., Ohmuro, M., Churchill, S.W. and Lior, N., 1995, 'Numerical calculations of laminar and turbulent natural convection in water in rectangular channels heated and cooledisothermally on the opposing vertical walls', *Int. J. Heat Mass Transfer*, vol. 28, no. 1, pp. 125-138.

[15] Sammouda, H. and Belghith, A., 1999, 'Finite element simulation of transient natural convection of low-Prandtl-number fluids in heated cavity', *Int. J Numerical Methods for Heat and Fluid Flow*, vol. 9, no. 5, pp. 612-624.